View Article Online
View Journal

Energy & Environmental Science

This article can be cited before page numbers have been issued, to do this please use: K. Krishnamoorthy, P. Pazhamalai and S. Kim, *Energy Environ. Sci.*, 2018, DOI: 10.1039/C8EE00160J.

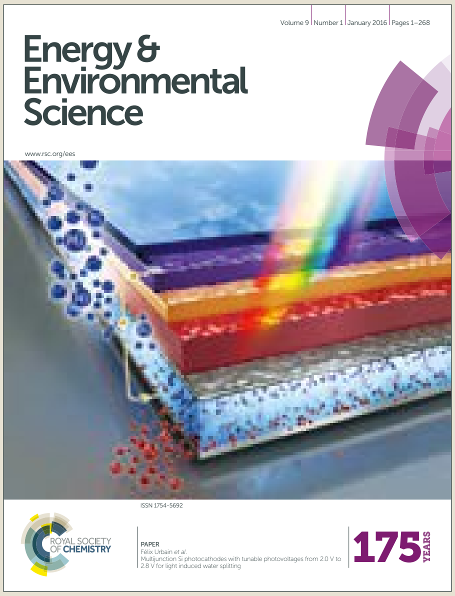

Volume 9 | Number 1 | January 2016 | Pages 1–268

Energy & Environmental Science

www.rsc.org/ees

ISSN 1754-5692

ROYAL SOCIETY OF CHEMISTRY

PAPER
Felix Urbain et al.
Multijunction Si photocathodes with tunable photovoltages from 2.0 V to 2.8 V for light induced water splitting

175 YEARS

View Article Online
DOI: 10.1039/C8EE00160J

Journal Name

ARTICLE

Two-dimensional siloxene nanosheets: Novel high-performance supercapacitor electrode materials

Karthikeyan Krishnamoorthy,[a] Parthiban Pazhamalai,[a] and Sang Jae Kim,[a,b,*]

Received 00th January 20xx,
Accepted 00th January 20xx

DOI: 10.1039/x0xx00000x

www.rsc.org/

Silicon-based materials have attracted considerable interest for the development of energy storage devices because of their ease of integration with existing silicon semiconductor technology. Herein, we have prepared siloxene sheets—a two-dimensional (2D) silicon material—and investigated their energy storage properties via fabrication of a symmetric supercapacitor (SSC) device containing 0.5 M tetraethylammonium tetrafluoroborate as the electrolyte. The formation of 2D siloxene sheets functionalized with oxygen, hydrogen, and hydroxyl groups was confirmed through X-ray diffraction, X-ray photoelectron spectroscopy, high-resolution transmission electron microscopy, and laser Raman mapping analyses. Cyclic voltammetric studies of the siloxene SSC device revealed the presence of pseudocapacitance in the siloxene sheets that arose from an intercalation/deintercalation phenomenon. The galvanostatic charge–discharge profiles of the device displayed sloped symmetric triangular curves with a maximum specific capacitance of 2.18 mF cm^{-2}, high energy density of 9.82 mJ cm^{-2}, good rate capability, and excellent cycling stability of 98% capacitance retention after 10,000 cycles. The siloxene SSC device delivered a maximum power density of 272.5 mW cm^{-2}, which is higher than those of other silicon- and carbon-based SSCs, highlighting their potential for application in energy storage.

1.Introduction

Increasing energy consumption needs and the fossil fuel crisis drive the development of high-performance energy storage and delivery systems[1,2]. Supercapacitors or electrochemical capacitors are an ideal choice for energy storage devices, mainly because of their high power density, high rate capability, and long cycle life[3,4]. To increase the energy/power ratio of supercapacitors, researchers have focused on the design and development of novel electrode materials[5–7]. In this regard, two-dimensional (2D) materials have received great consideration for the development of next-generation energy storage devices[8,9]. Since the advent of graphene sheets, multiple 2D materials including transition metal dichalcogenides (TMDs) like molybdenum disulfide (MoS_2), vanadium disulfide (VS_2), molybdenum diselenide ($MoSe_2$), and titanium disulfide (TiS_2), as well as MXenes, germanene, and phosphorene have been developed, and research on the energy storage properties of these materials is ongoing[10–14]. The fundamental charge storage properties of these materials for supercapacitor and battery applications have been examined over the past decade. However, the usefulness of these materials for on-chip energy storage micro-devices is still questionable because of the current limitations of direct integration on silicon-based materials, which are commonly used in microelectronic devices, wireless sensor networks, and implantable biomedical devices[15–17]. To solve this issue, it is necessary to develop an alternative material that is compatible with current silicon (Si) fabrication technology. It is anticipated that silicon-based materials for microcapacitors will be a suitable choice to aid integration with current microelectronic device technologies compared with conventional carbon-based materials such as onion-like carbon, carbon nanotubes, graphene, carbide-derived carbon, and diamond foam[16,18–20]. Therefore, silicon-based materials such as silicon thin films, nanowires, nanotrees, porous silicon, amorphous silicon, and their composites/hybrid materials have been examined for various electronic device applications including batteries, supercapacitors, and microcapacitors[16,21,22].

In this scenario, siloxene sheets prepared via deintercalation of calcium from calcium silicide ($CaSi_2$) are an exciting material because of their direct bandgap and 2D structure consisting of Si chains connected to surface-terminated functional groups that are mainly oxygen, hydrogen, and hydroxyl moities[23]. An earlier study demonstrated that the structure of siloxene sheets strongly depends on experimental conditions such reaction time, reaction medium, and temperature[24,25]. Different chemical structures of siloxene have been proposed such as the Weiss structure ($Si_6(OH)_3H_3$, in which alternating Si-H and Si-OH bonds are present on the surface of Si_6 rings), chain-like siloxene (oxygen incorporated in the Si planes leading to Si wires), and Kautsky structure ($Si_6O_3H_6$, in which Si_6 rings are connected through Si–O–Si bridges)[25–27]. Deak et al.[28] demonstrated that oxygen incorporation in a planar silicon matrix results in a quantum confinement effect, which is responsible for its luminescence. A theoretical study on siloxene sheets demonstrated their promise for applications in solar–electric energy conversion and

---

[a] Department of Mechatronics Engineering, Jeju National University, Jeju 63243, Republic of Korea.
[b] Department of Advanced Convergence Science and Technology, Jeju National University, Jeju 63243, Republic of Korea. Email: kimsangj@jejunu.ac.kr

† Footnotes relating to the title and/or authors should appear here.

Electronic Supplementary Information (ESI) available: [details of any supplementary information available should be included here]. See DOI: 10.1039/x0xx00000x

View Article Online
DOI: 10.1039/C8EE00160J

water splitting[29]. Siloxene nanosheets have been experimentally explored as a metal-free semiconductor for efficient water-splitting reactions even in the absence of a sacrificial reagent[30]. Similarly, siloxene sheets and their calcium bridged hybrids are an excellent lithium (Li)-storage anode material in Li-ion batteries[31]. Fu et al. reported the reversible Li-ion storage in siloxene with a specific capacity of 500 mAh g^{-1} [32]. They also examined the effect of carbon coating on the silicon-based suboxides derived from siloxene, which resulted in improved electrochemical properties with a high specific capacity of 946 mAh g^{-1}.

Being a planar Si structure with S_6 rings interconnected with various functional groups, large interlayer spacing, and high surface area, we envisaged that siloxene sheets could be an ideal candidate for supercapacitor applications. From this perspective, in this work, we explore the electrochemical capacitive properties of siloxene sheets by fabricating a symmetric supercapacitor (SSC) using tetraethylammonium tetrafluoroborate ($TEABF_4$) as the electrolyte. Few studies have reported the electrochemistry of siloxene sheets; here we demonstrate the potential of siloxene sheets as a high-performance electrode material for supercapacitors.

2. Results and discussion

Figure 1(A–C) show schematic representations of the topotactic transformation of layered $CaSi_2$ into 2D siloxene sheets using ice-cold hydrochloric acid (HCl)[25,32]. The slow dissolution of calcium in HCl solution, releasing hydrogen gas, and functionalization of siloxene sheets with OH groups occur simultaneously during the reaction, which can be observed visually as a color change of the reaction medium[25]. Figure S1, electronic supplementary information (ESI) shows a digital photograph of the $CaSi_2$ powder and siloxene sheets indicating a change in color from black to green, thus confirming the formation of siloxene sheets via deintercalation of calcium from $CaSi_2$[30].

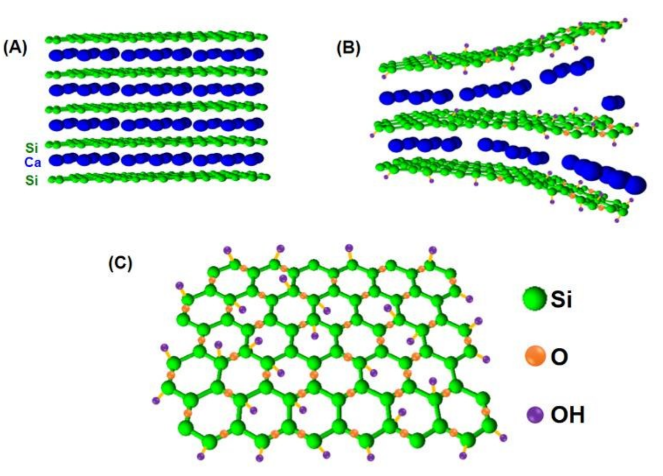

Figure 1 Schematic representation of the preparation of siloxene sheets. (A) Structure of $CaSi_2$, (B) transformation of layered $CaSi_2$ into siloxene sheets through topochemical reaction, and (C) structure of the resulting siloxene sheets.

To identify the structure of the siloxene sheets, the X-ray diffraction (XRD) pattern of the siloxene sheets was compared with that of $CaSi_2$ (Fig. S2, ESI). The XRD pattern of $CaSi_2$ contains sharp diffraction peaks that are in good agreement with JCPDS card no. 75-2192. After the topotactic reaction, the XRD pattern of the siloxene sheets (given in Fig. 2(A)) differed from that of $CaSi_2$ as follows: (i) the diffraction peaks corresponding to $CaSi_2$ almost completely disappeared, and (ii) two new peaks appeared at $2\theta = 13.5°$ and 26°. The diffraction peaks observed at 13.5° and 26° correspond to the (001) and (100) planes of 2D silicon derived from $CaSi_2$ with a hexagonal unit cell, in good agreement with previous studies[25,33]. The type of functional groups in the siloxene sheets was characterized using Fourier transform infrared (FT-IR) spectroscopy, as shown in Fig. 2(B). The FT-IR spectrum of the siloxene sheets displayed sharp and broad bands compared with those of $CaSi_2$ (Fig. S3, ESI). The bands observed at 452, 867, 1034, 1639, and 2140 cm^{-1} correspond to the vibrations of ν(Si-Si), ν(Si-H), ν(Si-O-Si), ν(Si-OH), and $\nu(OSi_2 \equiv Si\text{-}H)$, respectively[31]. The presence of $\nu(OSi_2 \equiv Si\text{-}H)$ suggests that the siloxene sheets have a Kautsky-type structure in which Si planes mainly consisting of Si_6 rings are interconnected via Si-O-Si bridges[25]. The broad band observed at 3400 cm^{-1} corresponds to the hydroxyl groups present on the siloxene sheets formed by oxidation and hydroxylation during the topotactic reaction[31,34].

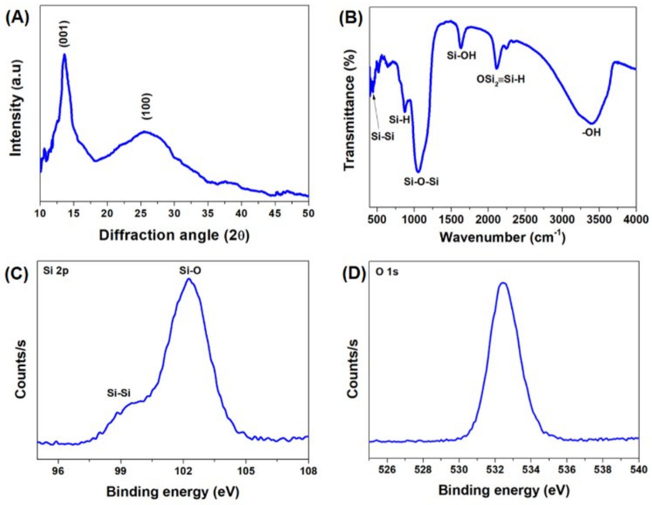

Figure 2 Physicochemical characterization of siloxene sheets. (A) X-ray diffraction pattern of the siloxene sheets. (B) Fourier transform infrared spectrum of the siloxene sheets. Core-level X-ray photoelectron spectra of siloxene sheets: (C) Si 2p states and (D) O 1s states.

The changes of the chemical states of the elements present in the siloxene sheets were compared with those of $CaSi_2$ through X-ray photoelectron spectroscopic analysis. The comparative XPS survey scans of $CaSi_2$ and the siloxene sheets are provided in Fig. S4 (ESI). The spectra confirm the presence of Ca and Si in $CaSi_2$ and the disappearance of Ca from the siloxene sheets. The core-level spectra of Ca and Si present in $CaSi_2$ are provided in Fig. S5 (ESI) and their binding energies are in agreement with reported values[35]. Figure 2(C) displays the core-level spectrum of the Si 2p states of siloxene sheets, which has two peaks at 99 and 103 eV. The former peak corresponds to the Si 2p states of Si-Si bonds in the siloxene sheets, and the latter to the oxygenated and hydrogenated counterparts of siloxene sheets[30]. Comparing the Si 2p states of $CaSi_2$ and siloxene (Fig. S6,

View Article Online
DOI: 10.1039/C8EE00160J

ESI), the peak observed at 97 eV originating from Ca-Si bonds in $CaSi_2$ was diminished and a new peak appeared around 99 eV, suggesting the formation of 2D siloxene sheets via topotactic reaction[36]. Figure 2(D) presents the O 1s spectrum, which contains a broad peak around 531 eV related to the oxygen- and hydroxyl-functionalized siloxene sheets[30,32]. The O/Si atomic ratio of the siloxene sheets determined from the XPS analysis is 1.39, which is in agreement with the recent findings of Fu and colleagues[32].

The surface morphology of the siloxene sheets was examined by field-emission scanning electron microscopy (FE-SEM) and high-resolution transmission electron microscopy (HR-TEM) with elemental mapping analysis. The FE-SEM images obtained at different magnifications (Fig. S7(A, B), ESI) revealed the sheet-like structures of siloxene with folded and crumpled regions at the edges. Figure 3(A) shows an HR-TEM image of siloxene, which illustrates its sheet-like morphology with lateral dimensions in the range of ~0.5 × 1 µm. Figure 3(B, C) depict the elemental mapping images of Si and O atoms in the siloxene sheets (obtained from energy dispersive spectroscopy (EDS) analysis), which indicated the homogeneous distributions of Si and O throughout the siloxene sheet. The EDS spectrum and composition analysis of the siloxene sheets (Fig. S8(A, B), ESI) revealed the presence of Si and O atoms in the siloxene sheets with an O/Si atomic ratio of about 1.49. The HR-TEM images in Fig. 3(D, E) revealed that the siloxene sheets consisted of a few layers, whereas the selected-area electron diffraction pattern in the inset of Fig. 3(E) highlights the amorphous nature of the siloxene sheets. Figure 3(F) and Fig. S9 (ESI) show atomic force microscopy (AFM) images of the siloxene sheets dispersed on a mica substrate. These images depict ultrathin sheets with a thickness in the range of 7 to 20 nm, as obtained from the section analysis of different sheets provided in Fig. S10 (ESI).

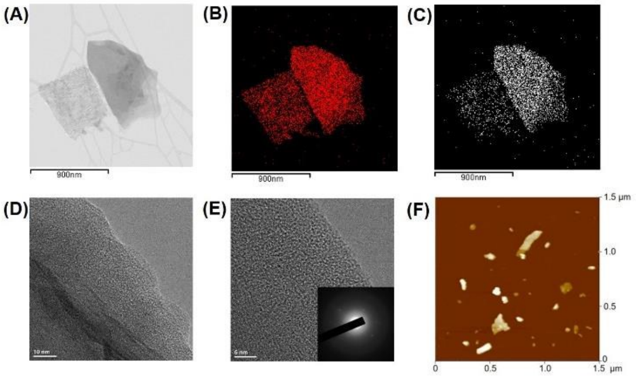

Figure 3 Surface morphology and elemental analysis of siloxene sheets. (A) High-resolution transmission electron microscopy (HR-TEM) images of the siloxene sheets. Elemental mapping of (B) Si atoms and (C) oxygen atoms in the siloxene sheets. (D) and (E) HR-TEM images of siloxene obtained at high magnification. The inset in (E) is the selected-area electron diffraction pattern of the siloxene sheets, which illustrates their amorphous nature. (F) Tapping-mode atomic force micrograph of the siloxene sheets.

Laser Raman spectroscopy and mapping are prominent tools to investigate the crystalline nature, defects, and role of functionalization in 2D materials such as graphene and TMDs[37]. Raman spectra of the siloxene sheets are presented in Fig. 4(A), which confirms the presence of Si-Si, Si-O, and Si-H groups. Compared with the Raman spectrum of $CaSi_2$ (provided in Fig. S11, ESI), the sharp band observed at 515 cm^{-1} broadened and split into two bands at 495 and 525 cm^{-1}, which are attributed to the vibrations of Si-O (495 cm^{-1}) and Si-Si (520 cm^{-1}) bonds, respectively[30,38]. The weak band observed at 375 cm^{-1} was attributed to Si-Si vibrations and those at 640 and 740 cm^{-1} are consistent with Si-H vibrations[30]. To understand the nature of the Si-O and Si-Si vibrational modes in more detail, Raman mapping analysis was performed. The peak position maps of Si-O and Si-Si vibrations are provided in Fig. 4(B) and (C), respectively. The Si-O band position varies from 495 to 505 cm^{-1}, as denoted by the red (495 cm^{-1}), pink (500 cm^{-1}), and yellow (505 cm^{-1}) regions in the map in Fig. 4(B). The peak position map of the Si-Si band in Fig. 4 (C) indicates the peak shifts from 518 to 526 cm^{-1}, which can be visualized from the green, red, pink, and yellow regions. In general, the Si-O and Si-Si signals correspond to the amorphous and crystalline domains in the siloxene sheets, respectively. Therefore, the Si-O/Si-Si intensity ratio map of siloxene sheets was constructed to understand the interconnection of Si-O with the Si_6 ring of siloxene; the map is shown in Fig. 4(D). The Si-O/Si-Si intensity ratio map revealed the variation of intensity ratio from 0.3 to nearly 2.0 over the mapped region, suggesting that Si-O is heterogeneously bridged over the Si_6 rings of siloxene[30,39].

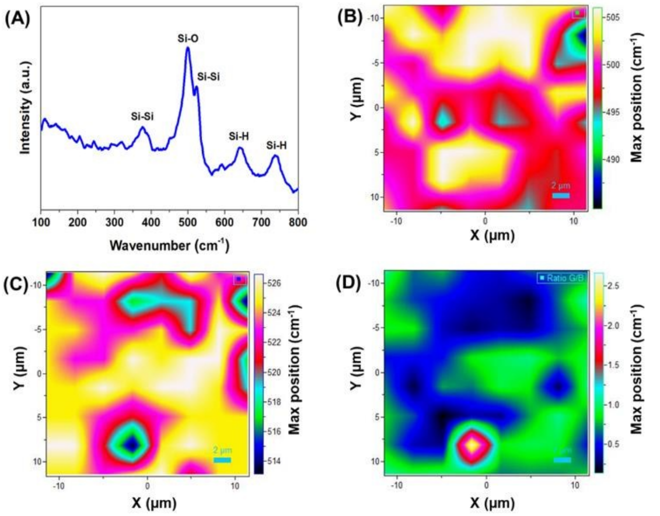

Figure 4 (A) Laser Raman spectrum of siloxene sheets revealing the presence of functional groups attached to the 2D silicon (Si_6) rings. Laser Raman mapping of the siloxene sheets including (B) the peak position map of Si-O vibrations observed at 495 cm^{-1}, (C) the peak position map of Si-Si vibrations observed at 525 cm^{-1}, and (D) the intensity ratio map of Si-O and Si-Si peaks.

The transformation of layered $CaSi_2$ into siloxene sheets via deintercalation of calcium was also studied through surface area and pore size analyses. Figure S12 (ESI) shows the N_2 adsorption–desorption isotherm of $CaSi_2$, from which it is clear that the surface area of $CaSi_2$ is about 2.12 m^2 g^{-1} and it does not contain any large pores. Figure S13(A) (ESI) presents the N_2 adsorption–desorption isotherm of the siloxene sheets, which contains hysteresis in the relative partial pressure region of 0.1 to 0.95. The isotherm observed for the siloxene sheets is a type-IV curve according to the IUPAC classification, and this result indicates the presence of mesopores[40]. The measured surface area of the siloxene sheets is 59.72 m^2 g^{-1} and the average pore size is about 4.0 Å (Fig. S13(B), ESI). The high surface area of the siloxene sheets originating from the presence of mesopores should improve their electrochemical properties.

View Article Online
DOI: 10.1039/C8EE00160J

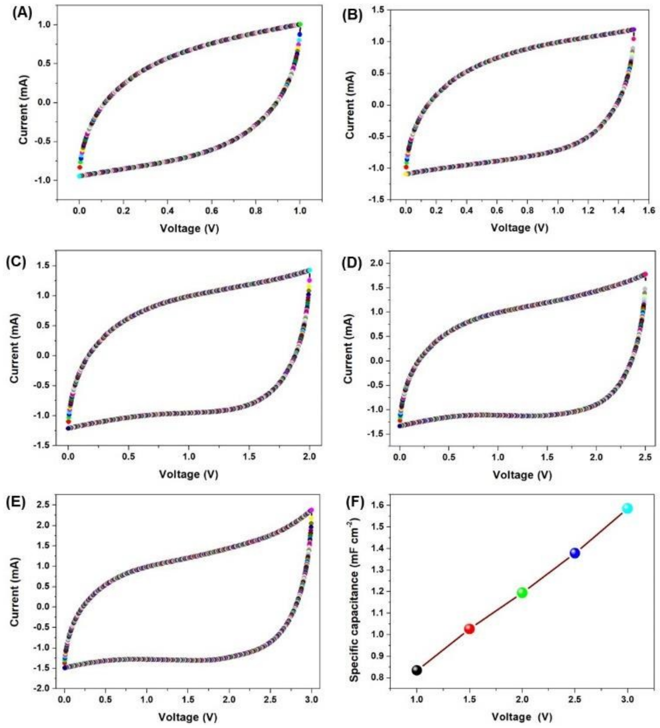

Figure 5 Electrochemical analysis of the siloxene-based symmetric supercapacitor device (CR2032 coin cell) in 0.5 M TEABF$_4$. (A–E) cyclic voltammetric profiles of the siloxene SSC device measured at operating voltages of 1.0 to 3.0 V using a scan rate of 400 mV s^{-1}. (F) Plot of specific capacitance against the operating potential window.

The electrochemical capacitive properties of the siloxene sheets were investigated in a SSC CR2032 coin cell configuration using 0.5 M TEABF$_4$ as the electrolyte. To determine the operating potential window (OPW) of the siloxene SSC device, cyclic voltammetric (CV) analysis was performed at different OPWs from 1.0 to 3.0 V at a scan rate of 400 mV s^{-1}; the results are shown in Fig. 5(A–E). Typical rectangular-like CV profiles were obtained at different OPWs, which evidenced that the siloxene SSC device can operate over an OPW of 3 V without any sign of degradation. Figure 5(F) shows the linear increase in the specific capacitance of siloxene with widening OPW from 1.0 to 3.0 V, which indicated the good electrochemical stability of the siloxene SSC device[41]. To understand the charge storage behavior in the siloxene SSC, CV measurements were conducted at different scan rates from 5 mV s^{-1} to 20 V s^{-1}, as presented in Fig. 6(A–C). The CV profiles measured at scan rates of 5 to 100 mV s^{-1} in Fig. 6(A) are quasi-rectangular with small redox peaks. The observed redox peaks might be caused by the intercalation and deintercalation of electrolyte ions into the siloxene sheets, similar to that observed for porous silicon and Ti$_3$C$_2$ MXenes[42,43]. Increasing the scan rate from 100 mV s^{-1} to 20 V s^{-1} resulted in an increase in current range and no redox peaks were observed at high scan rates, as shown in Fig 6(B) and (C). The rectangular shape of the CV profiles is retained even at high scan rates (above 200 mV s^{-1}), suggesting the high rate capability of the siloxene SSC device. Figure 6(D) presents a plot of specific capacitance against scan rate, which showed that the siloxene SSC device possesses an areal specific capacitance of 4.91 mF cm^{-2} at a scan rate of 5 mV s^{-1}. Further, the siloxene SSC device delivered a specific capacitance of about 2.12 mF cm^{-2} as the scan rate increased by about 20 times. At a very high scan rate of about 20 V s^{-1}, the siloxene SSC device still displayed a specific capacitance of about 219 μF cm^{-2}, suggesting the good rate capability of the siloxene sheets[44].

Electrochemical impedance spectroscopy (EIS) was used to evaluate the charge-storage behavior in the siloxene SSC device using Nyquist and Bode plots. The Nyquist plot presented in Fig. 6(E) contains low-, intermediate-, and high-frequency regions that correspond to the synchronous charging, asynchronous charging, and non-charging regions of the siloxene SSC device, respectively[45]. In the low-frequency region, the vertical line almost parallel to the y-

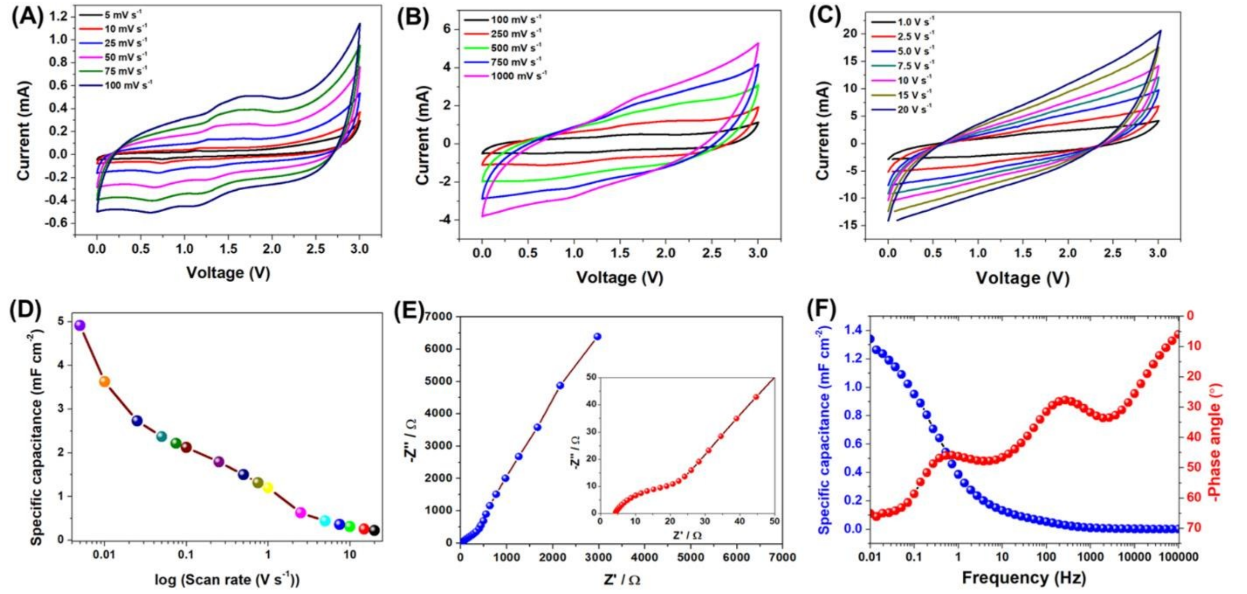

Figure 6 Electrochemical analysis of the siloxene-based symmetric supercapacitor device (CR2032 coin cell) in 0.5 M TEABF$_4$. (A–C) Cyclic voltammetric profiles measured at scan rates from 5 mV s^{-1} to 20 V s^{-1}. (D) Variation of areal specific capacitance with respect to scan rate. (E) Nyquist plot; the inset shows an enlarged area of the high-frequency region. (F) Dependence of specific capacitance and phase angle on applied frequency.

View Article Online
DOI: 10.1039/C8EE00160J

axis indicate the capacitive behavior of the siloxene SSC device. The intermediate region with a slope of 45° is dominated by the presence of pores that possess a wide range of time constants, thus resulting in the asynchronous charging behavior of the siloxene SSC device. In the high-frequency region, a well-defined semi-circular arc is observed that originates from the resistance between the electrolyte and electrode materials[46]. The determined equivalent series resistance of the siloxene SSC device is 4.379 Ω, which results in a maximum power density of about 272.5 mW cm^{-2}. The maximum power density of the siloxene SSC device is higher than those reported for silicon- and carbon-based SSCs such as silicon nanowire microcapacitors (182 mW cm^{-2})[15], silicon nanowires with a length of 10 µm (1.6 mW cm^{-2})[47], silicon nanotrees (235 mW cm^{-2})[48], carbon microcapacitors on a silicon substrate (34.4 mW cm^{-2})[49], and onion-like carbon-based microcapacitors (240 mW cm^{-2})[19], respectively. These results substantiate that siloxene-based devices are an attractive alternative to carbon-based devices for microelectronics because of their higher power density. Figure 6(F) shows that the specific capacitance of the siloxene SSC device decreases with a corresponding increase in frequency and the device behaves like a resistor in the high-frequency region [40]. A specific capacitance of 1.33 mF cm^{-2} was obtained for the siloxene SSC device at a low frequency of about 0.01 Hz. The Bode phase angle plot in Fig. 6(F) shows that the phase angle in the low-frequency region is about −65°. For ideal capacitors, the phase angle will be close to −90°, whereas it will be closer to −45° for pseudocapacitors[46]. This result revealed the presence of intercalation capacitance in the siloxene SSC. Furthermore, the capacitor response frequency (f_o) at a phase angle of −45° was 13.89 Hz. Thus, the calculated relaxation time of the siloxene SSC device is 71 ms, which is comparable to the values reported for silicon- and carbon-based supercapacitors[50].

The galvanostatic charge–discharge (CD) profile of the siloxene SSC device obtained at a constant current of 0.5 mA is displayed in Fig. 7(A), which shows the presence of quasi-symmetric CD behavior. Figure 7(B) presents the CD profiles of the siloxene SSC device measured at different current ranges. Symmetric profiles were obtained at high current, whereas sloped symmetric profiles were observed at low current, which is consistent with the CV profiles at low scan rates. Figure 7(C) shows the effect of discharge current on the specific capacitance of the siloxene SSC device. Specific capacitance increased with decreasing discharge current. The siloxene SSC device delivered an areal specific capacitance of 2.18 mF cm^{-2} (gravimetric capacitance of about 4.06 F g^{-1}) at a current of 0.25 mA. The specific capacitance of the siloxene SSC device is higher than those of reported silicon-based SSC devices (Table S1, ESI), such as silicon nanowires (30 µF cm^{-2})[15], silicon nanotrees (1.7 mF cm^{-2})[48], silicon nanowires with a length of 50 µm (0.44 mF cm^{-2}) [51], porous silicon (0.5 mF cm^{-2})[52], and diamond-coated silicon nanowires (0.4 mF cm^{-2})[53]. The areal and gravimetric specific capacitances of the siloxene SSC device are also compared with the corresponding values for recently developed layered TMDs in Table S2 and S3 (ESI). The areal capacitance of the siloxene SSC device with TEABF$_4$ as the electrolyte of 2.18 mF cm^{-2} over an OPW from 0.0 to 3.0 V is comparatively higher than those of exfoliated MoS$_2$-based SSC devices with Et$_4$NBF$_4$ (OPW from 1.0 to 1.7 V) and BMIM-PF$_6$ (OPW from −2.0 to 1.5 V) as electrolytes of 2.25 and 2.4 mF cm^{-2}, respectively[54]. Table S3 (ESI) shows that the siloxene SSC device possesses a high gravimetric capacitance of 4.06 F g^{-1}, which is larger than those of SSC devices (with aqueous electrolytes) based on graphene sheets, layered TMDs, and MXenes[55,56]. High rate capability is one of the most important features of supercapacitors. Figure 7(D) depicts the rate capability of the siloxene SSC device. The device exhibits stable cycling at all currents from 0.5 to 10 mA and is reversible with good retention when cycling is switched from low to high current range and vice versa. Thus, the siloxene SSC device is capable of delivering energy at various load levels, which is one of the important features of supercapacitors.

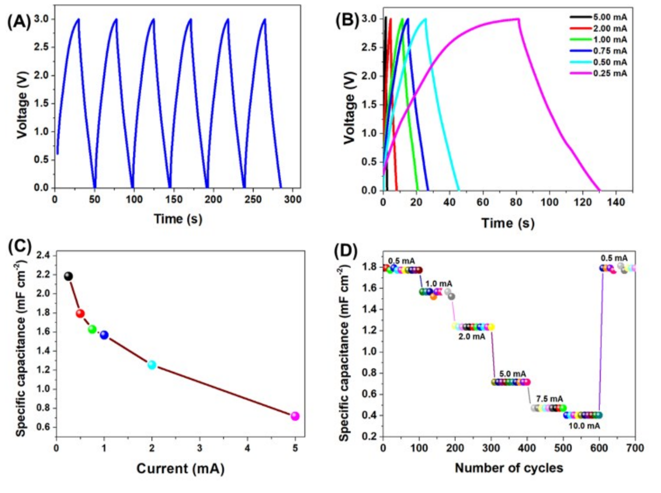

Figure 7 (A) Galvanostatic charge–discharge profiles of the siloxene supercapacitor device measured at a constant current of 0.5 mA. (B) Charge–discharge profiles obtained in various current ranges. (C) Effect of discharge current on the areal specific capacitance of the siloxene supercapacitor device. (D) Rate capability of the siloxene supercapacitor device.

The energy density, power density, and cycling stability of a supercapacitor are some of the important factors determining its practical application[2,57]. The energy and power densities of the siloxene SSC device were calculated from the CD profiles; Ragone plots are provided in Fig. 8(A) and Fig. S15 (ESI). These plots demonstrated that the siloxene SSC device delivered an energy density of about 9.82 mJ cm^{-2} (gravimetric energy density of 5.08 Wh Kg^{-1}) at a constant current of 0.25 mA with a corresponding power density of 0.2 mW cm^{-2}. The energy density of the siloxene SSC device decreased from 9.82 to 3.22 mJ cm^{-2} (5.08 to 1.46 Wh Kg^{-1}) with an increase of power density from 0.2 to 4.03 mW cm^{-2} (375 to 7500 W Kg^{-1}) as the galvanostatic discharge current range increased from 0.25 to 5 mA. Figure 8(A) illustrates the superior performance of the siloxene SSC device compared with those of graphene-, MXenes-, and silicon-based supercapacitor systems[15,17,22,48,58–65]. The siloxene SSC device displays higher power density than those of other supercapacitors based on Si nanowires (1–2 mW cm^{-2})[15], highly doped Si nanowires (1.6 mW cm^{-2})[47], polypyrrole (0.56 mW cm^{-2})[66], PEDOT-coated Si nanowires (0.8 mW cm^{-2})[67], MnO$_2$ nanoflakes on Si nanowires (1 mW cm^{-2})[68], and Si nanowires coated with RuO$_2$ (0.17 mW cm^{-2})[65]. Table S2 and S3 (ESI) reveal that the areal and gravimetric performances of the siloxene SSC device are comparable with those of SSCs with graphene, MXenes, MoS$_2$, MoSe$_2$, SnSe, and GeSe$_2$ electrodes[56,64,69,70].

View Article Online
DOI: 10.1039/C8EE00160J

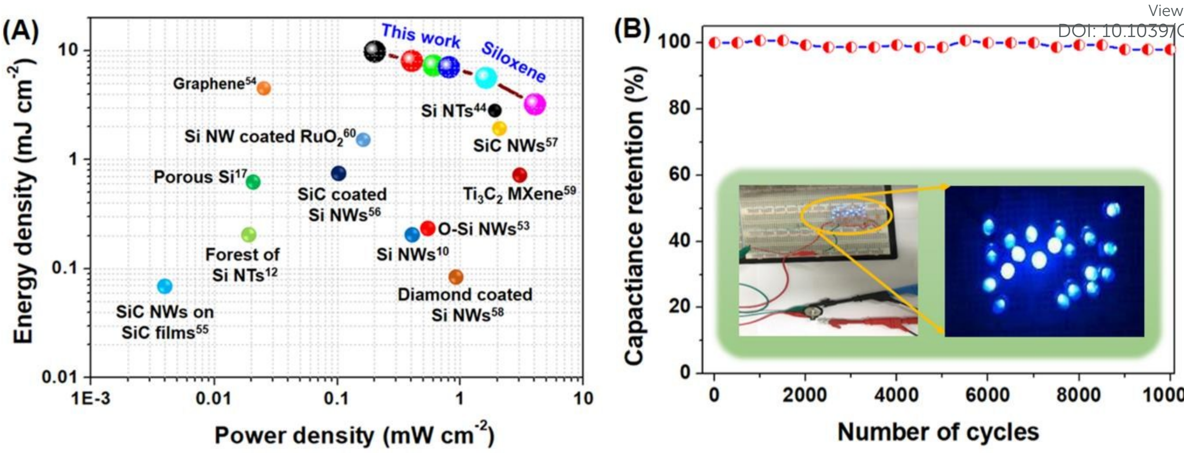

Figure 8 (A) Ragone plot representing the dependence of the energy density of the siloxene supercapacitor device on power density. (B) Cycling stability of the siloxene supercapacitor device over 10,000 charge–discharge cycles. The inset in (B) shows a practical application of the fully charged siloxene supercapacitor device delivering enough energy to glow 20 commercial LEDs.

The superior performance metrics of the siloxene SSC over other related devices can be ascribed to the following factors: (i) the conductive hexagonal silicon framework (Fig. 1(C)) of the siloxene sheets facilitates both ion diffusion and electron transfer kinetics at the surfaces, (ii) the large interlayer spacing between the individual sheets caused by the presence of functional groups (see Fig. 2(B)) provides large active sites for ion intercalation/deintercalation reactions, (iii) the high surface area (59.72 $m^2\ g^{-1}$) and wide pore size distribution of the siloxene sheets provide fast ion transport kinetics throughout the available surface of the sheets, and (iv) use of $TEABF_4$ as the electrolyte in the SSC provides a wide OPW, which is important to increase the energy density of supercapacitors. Figure 8(B) presents the cycling stability of the siloxene SSC device over 10000 CD cycles at a current of 2 mA. The siloxene SSC device exhibited a capacitance retention of about 98% after 10000 cycles, suggesting its excellent cycling stability and electrochemical reversibility. The inset of Fig. 8(B) demonstrates a practical application of the fabricated siloxene SSC device. The device was charged to 3.0 V and then the stored energy was delivered to light up 20 LEDs for nearly 15 s. Altogether, these results demonstrated the promise of the fabricated siloxene SSC for use in next-generation energy storage applications.

Conclusions

We prepared 2D siloxene sheets via topotactic transformation of $CaSi_2$ in ice-cold HCl and demonstrated its high-rate energy storage properties. An SSC device based on the siloxene sheets operated over a wide potential range of 3.0 V with a maximum specific capacitance of 2.18 mF cm^{-2}, high energy density of 9.82 mJ cm^{-2}, and good rate capability. The siloxene SSC device displayed a maximum power density of 272.5 mW cm^{-2}, which is higher than those of other silicon- and carbon-based supercapacitors. The siloxene SSC device showed excellent cycling stability with about 98% capacitance retention after 10,000 CD cycles. Considering the achieved electrochemical performance and demonstrated practical application of the 2D siloxene-based SSC device, we strongly believe that siloxene sheets are a promising electrode material for next-generation energy storage devices.

Conflicts of interest

"There are no conflicts to declare".

Acknowledgements

This research was supported by the Basic Science Research Program through the National Research Foundation of Korea (NRF) funded by the Ministry of Science, ICT & Future Planning (2016R1A2B2013831 and 2017R1C1B2012784).

Notes and references

‡ Electronic supplementary information (ESI) associated with this paper contains experimental section, instrumentation, electrochemical method and analysis, physico-chemical characterization of $CaSi_2$ (XRD patterns, FT-IR spectra, XPS data, a laser Raman spectrum), N_2 adsorption/desorption isotherms of $CaSi_2$ and siloxene, and performance metrics of siloxene SSC device with the reported ones.

References

1 A. M. Elshahawy, C. Guan, X. Li, H. Zhang, Y. Hu, H. Wu, S. J. Pennycook and J. Wang, *Nano Energy*, 2017, **39**, 162–171.
2 S. Zhang and N. Pan, *Adv. Energy Mater.*, 2015, **5**, 1401401.
3 J. Y. Hwang, M. Li, M. F. El-Kady and R. B. Kaner, *Adv. Funct. Mater.*, 2017, **27**, 1605745.
4 T. Qin, S. Peng, J. Hao, Y. Wen, Z. Wang, X. Wang, D. He, J. Zhang, J. Hou and G. Cao, *Adv. Energy Mater.*, 2017, **7**, 1700409.
5 X. Geng, Y. Zhang, Y. Han, J. Li, L. Yang, M. Benamara, L. Chen and H. Zhu, *Nano Lett.*, 2017, **17**, 1825–1832.
6 Z. Xiong, C. Liao, W. Han and X. Wang, *Adv. Mater.*, 2015, **27**, 4469–4475.
7 C. Zhang, Y. Huang, S. Tang, M. Deng and Y. Du, *ACS Energy Lett.*, 2017, **2**, 759–768.
8 X. Zhang, L. Hou, A. Ciesielski and P. Samorì, *Adv. Energy Mater.*,

View Article Online
DOI: 10.1039/C8EE00160J

2016, **6**, 1600671.
9 A. H. Khan, S. Ghosh, B. Pradhan, A. Dalui, L. K. Shrestha, S. Acharya and K. Ariga, *Bull. Chem. Soc. Jpn.*, 2017, **90**, 627–648.
10 K. Krishnamoorthy, P. Pazhamalai, G. K. Veerasubramani and S. J. Kim, *J. Power Sources*, 2016, **321**, 112–119.
11 Y. Wang, H. Dou, J. Wang, B. Ding, Y. Xu, Z. Chang and X. Hao, *J. Power Sources*, 2016, **327**, 221–228.
12 M. A. Bissett, S. D. Worrall, I. A. Kinloch and R. A. W. Dryfe, *Electrochim. Acta*, 2016, **201**, 30–37.
13 C. Hao, B. Yang, F. Wen, J. Xiang, L. Li, W. Wang, Z. Zeng, B. Xu, Z. Zhao, Z. Liu and Y. Tian, *Adv. Mater.*, 2016, **28**, 3194–3201.
14 H. Li, Y. Hou, F. Wang, M. R. Lohe, X. Zhuang, L. Niu and X. Feng, *Adv. Energy Mater.*, 2017, **7**, 1601847.
15 D. Aradilla, P. Gentile, G. Bidan, V. Ruiz, P. Gómez-Romero, T. J. S. Schubert, H. Sahin, E. Frackowiak and S. Sadki, *Nano Energy*, 2014, **9**, 273–281.
16 D. Aradilla, D. Gaboriau, G. Bidan, P. Gentile, M. Boniface, D. Dubal, P. Gomez-Romero, J. Wimberg, T. J. S. Schubert and S. Sadki, *J. Mater. Chem. A Mater. Energy Sustain.*, 2015, **3**, 13978–13985.
17 F. Thissandier, P. Gentile, T. Brousse, G. Bidan and S. Sadki, *J. Power Sources*, 2014, **269**, 740–746.
18 S. Chatterjee, R. Carter, L. Oakes, W. R. Erwin, R. Bardhan and C. L. Pint, *J. Phys. Chem. C*, 2014, **118**, 10893–10902.
19 P. Huang, D. Pech, R. Lin, J. K. McDonough, M. Brunet, P. L. Taberna, Y. Gogotsi and P. Simon, *Electrochem. commun.*, 2013, **36**, 53–56.
20 D. Aradilla, M. Delaunay, S. Sadki, J.-M. Gérard and G. Bidan, *J. Mater. Chem. A*, 2015, **3**, 19254–19262.
21 C. . Cui, Y. Lieber, *Science (80-.).*, 2001, **291**, 851–853.
22 A. P. Cohn, W. R. Erwin, K. Share, L. Oakes, A. S. Westover, R. E. Carter, R. Bardhan and C. L. Pint, *Nano Lett.*, 2015, **15**, 2727–2731.
23 H. Nakano, M. Ishii and H. Nakamura, *Chem. Commun. (Camb).*, 2005, **2**, 2945–2947.
24 H. Nakano, *J. Ceram. Soc. Japan*, 2014, **122**, 748–754.
25 M. I. Shoji Yamanaka, Hiroyuki Matsu-ura, *Mater. Res. Bull.*, 1996, **31**, 307–316.
26 J. R. Dahn, B. M. Way, E. Fuller and J. S. Tse, *Phys. Rev. B*, 1993, **48**, 17872–17877.
27 H. Oughaddou, H. Enriquez, M. R. Tchalala, H. Yildirim, A. J. Mayne, A. Bendounan, G. Dujardin, M. Ait Ali and A. Kara, *Prog. Surf. Sci.*, 2015, **90**, 46–83.
28 P. Deák, M. Rosenbauer, M. Stutzmann, J. Weber and M. S. Brandt, *Phys. Rev. Lett.*, 1992, **69**, 2531–2534.
29 K. Xu, L. Ben, H. Li and X. Huang, *Nano Res.*, 2015, **8**, 2654–2662.
30 S. Li, H. Wang, D. Li, X. Zhang, Y. Wang, J. Xie, J. Wang, Y. Tian, W. Ni and Y. Xie, *J. Mater. Chem. A*, 2016, **4**, 15841–15844.
31 H. Imagawa, N. Takahashi, T. Nonaka, Y. Kato, K. Nishikawa and H. Itahara, *J. Mater. Chem. A*, 2015, **3**, 9411–9414.
32 R. Fu, K. Zhang, R. P. Zaccaria, H. Huang, Y. Xia and Z. Liu, *Nano Energy*, 2017, **39**, 546–553.
33 H. Nakano, O. Ohtani, T. Mitsuoka, Y. Akimoto and H. Nakamura, *J. Am. Ceram. Soc.*, 2005, **88**, 3522–3524.
34 J. He, J. S. Tse, D. D. Klug and K. F. Preston, *J. Mater. Chem.*, 1998, **8**, 705–710.
35 A. Schöpke, R. Würz and M. Schmidt, *Surf. Interface Anal.*, 2002, **34**, 464–467.
36 H. NAKANO, *Solid State Ionics*, 1992, **53**–**56**, 635–640.
37 K. Krishnamoorthy, G. K. Veerasubramani, P. Pazhamalai and S. J. Kim, *Electrochim. Acta*, 2016, **190**, 305–312.
38 H. D. Fuchs, M. Stutzmann, M. S. Brandt, M. Rosenbauer, J. Weber, a Breitschwerdt, P. Deak and M. Cardona, *Phys. Rev. B*, 1993, **48**, 8172–8189.
39 M. S. Brandt, L. Hoppel, N. Zamanzadeh-Hanebuth, G. Vogg and M. Stutzmann, *Phys. Status Solidi B-Basic Res.*, 1999, **215**, 409–412.
40 K. Krishnamoorthy, P. Pazhamalai, S. Sahoo and S.-J. Kim, *J. Mater. Chem. A*, 2017, **5**, 5726–5736.
41 M. S. Javed, S. Dai, M. Wang, D. Guo, L. Chen, X. Wang, C. Hu and Y. Xi, *J. Power Sources*, 2015, **285**, 63–69.
42 A. S. . b Westover, D. . Freudiger, Z. S. . Gani, K. . b Share, L. . b Oakes, R. E. . Carter and C. L. . b Pint, *Nanoscale*, 2015, **7**, 98–103.
43 Z. Lin, D. Barbara, P. L. Taberna, K. L. Van Aken, B. Anasori, Y. Gogotsi and P. Simon, *J. Power Sources*, 2016, **326**, 575–579.
44 B. Xie, C. Yang, Z. Zhang, P. Zou, Z. Lin, G. Shi, Q. Yang, F. Kang and C. P. Wong, *ACS Nano*, 2015, **9**, 5636–5645.
45 J. Li, V. Mishukova and M. Östling, *Appl. Phys. Lett.*, 2016, **109**, 123901.
46 K. Krishnamoorthy, P. Pazhamalai and S. J. Kim, *Electrochim. Acta*, 2017, **227**, 85–94.
47 F. Thissandier, A. Le Comte, O. Crosnier, P. Gentile, G. Bidan, E. Hadji, T. Brousse and S. Sadki, *Electrochem. commun.*, 2012, **25**, 109–111.
48 D. Gaboriau, D. Aradilla, M. Brachet, J. Le Bideau, T. Brousse, G. Bidan, P. Gentile, S. Sadki, V. Calvo, S. Sadki and M. Chen, *RSC Adv.*, 2016, **6**, 81017–81027.
49 H. Durou, D. Pech, D. Colin, P. Simon, P.-L. Taberna and M. Brunet, *Microsyst. Technol.*, 2012, **18**, 467–473.
50 Y. G. Majid Beidaghi, *Energy Environ. Sci.*, 2014, **7**, 867–884.
51 F. Thissandier, P. Gentile, N. Pauc, T. Brousse, G. Bidan and S. Sadki, *Nano Energy*, 2014, **5**, 20–27.
52 D. S. Gardner, C. W. Holzwarth, Y. Liu, S. B. Clendenning, W. Jin, B.-K. Moon, C. Pint, Z. Chen, E. C. Hannah, C. Chen, C. Wang, E. Mäkilä, R. Chen, T. Aldridge and J. L. Gustafson, *Nano Energy*, 2016, **25**, 68–79.
53 D. Aradilla, F. Gao, G. Lewes-Malandrakis, W. Müller-Sebert, P. Gentile, S. Pouget, C. E. Nebel and G. Bidan, *Electrochim. Acta*, 2017, **242**, 173–179.
54 A. Winchester, S. Ghosh, S. Feng, A. L. Elias, T. Mallouk, M. Terrones and S. Talapatra, *ACS Appl. Mater. Interfaces*, 2014, **6**, 2125–2130.
55 M. A. Bissett, I. A. Kinloch and R. A. W. Dryfe, *ACS Appl. Mater. Interfaces*, 2015, **7**, 17388–98.
56 R. B. Rakhi, B. Ahmed, M. N. Hedhili, D. H. Anjum and H. N. Alshareef, *Chem. Mater.*, 2015, **27**, 5314–5323.
57 P. Pazhamalai, K. Krishnamoorthy, M. S. P. Sudhakaran and S. J. Kim, *ChemElectroChem*, 2017, **4**, 396–403.
58 N. Berton, M. Brachet, F. Thissandier, J. Le Bideau, P. Gentile, G. Bidan, T. Brousse and S. Sadki, *Electrochem. commun.*, 2014, **41**, 31–34.
59 A. Ramadoss, K.-Y. Yoon, M.-J. Kwak, S.-I. Kim, S.-T. Ryu and J.-H. Jang, *J. Power Sources*, 2017, **337**, 159–165.
60 J. P. Alper, M. S. Kim, M. Vincent, B. Hsia, V. Radmilovic, C. Carraro and R. Maboudian, *J. Power Sources*, 2013, **230**, 298–302.
61 J. P. Alper, M. Vincent, C. Carraro and R. Maboudian, *Appl. Phys. Lett.*, 2012, **100**, 163901.
62 L. Gu, Y. Wang, Y. Fang, R. Lu and J. Sha, *J. Power Sources*, 2013, **243**, 648–653.
63 F. Gao, G. Lewes-Malandrakis, M. T. Wolfer, W. Müller-Sebert, P. Gentile, D. Aradilla, T. Schubert and C. E. Nebel, *Diam. Relat. Mater.*, 2015, **51**, 1–6.
64 N. Kurra, B. Ahmed, Y. Gogotsi and H. N. Alshareef, *Adv. Energy Mater.*, 2016, **6**, 1601372.
65 W. Zheng, Q. Cheng, D. Wang and C. V. Thompson, *J. Power Sources*, 2017, **341**, 1–10.
66 W. Sun, R. Zheng and X. Chen, *J. Power Sources*, 2010, **195**, 7120–7125.
67 D. Aradilla, G. Bidan, P. Gentile, P. Weathers, F. Thissandier, V. Ruiz, P. Gómez-Romero, T. J. S. Schubert, H. Sahin and S. Sadki, *RSC Adv.*, 2014, **4**, 26462.
68 D. P. Dubal, D. Aradilla, G. Bidan, P. Gentile, T. J. S. Schubert, J. Wimberg, S. Sadki and P. Gomez-Romero, *Sci. Rep.*, 2015, **5**, 9771.

View Article Online
DOI: 10.1039/C8EE00160J

69 C. Zhang, H. Yin, M. Han, Z. Dai, H. Pang, Y. Zheng, Y.-Q. Lan, J. Bao and J. Zhu, *ACS Nano*, 2014, **8**, 3761–3770.
70 X. Wang, B. Liu, Q. Wang, W. Song, X. Hou, D. Chen, Y. Cheng and G. Shen, *Adv. Mater.*, 2013, **25**, 1479–1486.

View Article Online
DOI: 10.1039/C8EE00160J

Table of contents

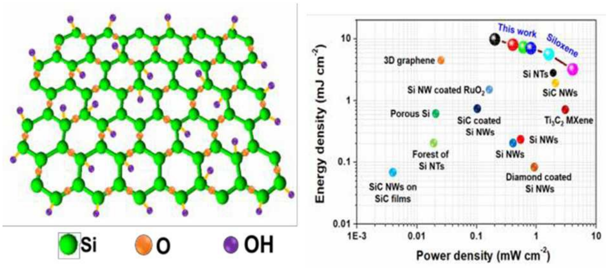

A symmetric supercapacitor constructed using two dimensional siloxene sheets in an ionic liquid electrolyte exhibits high areal capacitance and energy density.

View Article Online
DOI: 10.1039/C8EE00160J

Broader context (Manuscript ID: EE-ART-01-2018-000160.R1):

The development of supercapacitors with high energy/power ratio has been rapidly increasing due to their prospective applications in the electronics industry. Global research work has been focused on understanding the fundamental charge-storage mechanism and performance evaluation of novel materials for supercapacitors. Two dimensional nanostructures including graphene, layered transition metal dichalcogenides, and MXenes based electrodes showed superior supercapacitive properties during this decade. However, the integration of these materials/devices with existing silicon technology will be debatable or needs high cost. Thus, the development of silicon-based electrodes for supercapacitors is highly appreciable considering the ease of integration with silicon technology. Here, siloxene sheets (a 2D material comprising silicon sheets functionalized with oxygenated groups) were prepared via topochemical extraction of calcium from calcium silicide using hydrochloric acid and investigated as an electrode for supercapacitors utilizing ionic liquid electrolyte. The siloxene symmetric supercapacitor (SSC) device operates over a wide operating potential window, possesses high energy density with maximal power density (higher than reported silicon-based supercapacitors) as well as offers long lifetime. This study opens up new horizons towards the development of high performance supercapacitor by employing siloxene sheets.